Topological insulator path toward efficient hydrogen evolution catalysts in the Li_2Pt family

Yu-Hao Wei,[1] Da-Shuai Ma,[2,3,*] Hong-Kuan Yuan,[1] Xiaotian Wang,[1,4,†] and Min-Quan Kuang[1,‡]

[1]*Chongqing Key Laboratory of Micro & Nano Structure Optoelectronics, and School of Physical Science and Technology, Southwest University, Chongqing 400715, People's Republic of China*

[2]*Institute for Structure and Function & Department of Physics & Chongqing Key Laboratory for Strongly Coupled Physics, Chongqing University, Chongqing 400044, People's Republic of China*

[3]*Center of Quantum materials and devices, Chongqing University, Chongqing 400044, People's Republic of China*

[4]*Institute for Superconducting and Electronic Materials (ISEM), University of Wollongong, Wollongong 2500, Australia*

(Received 21 February 2023; accepted 8 June 2023; published 20 June 2023)

Topological materials, such as topological semimetals and topological insulators, with robust topological surface states have bright application prospects in electrochemical catalysis. Here, the first-principles calculations indicate the strong topological insulator Li_2Pt family promotes efficient catalytic response to the hydrogen evolution reaction. For Li_2Pt and Li_2Pd, the calculated Gibbs free energy ΔG_{H^*} of the bridge site is 0.054 eV and 0.041 eV, while that for the top site is 0.187 eV and 0.641 eV, respectively. The better hydrogen evolution reaction performance of the bridge site can ascribe to H hybridizes with the $d_{xy} + d_{x^2-y^2}$ orbital, which donates the nontrivial topological surface states, while H hybridizes with the d_{z^2} orbital that withholds contribution to topological surface states for the top site. Noticeably, the ΔG_{H^*} of the bridge site for Li_2Pt (0.054 eV) and Li_2Pd (0.041 eV) is nearly half of the value of Pt (0.09 eV), indicating an excellent hydrogen evolution reaction activity. This work uncovers the hybridization between adsorbate and topological surface states plays a vital role in enhancing the hydrogen evolution reaction performance and provides a promising route to design topological quantum catalysts.

DOI: 10.1103/PhysRevB.107.235414

I. INTRODUCTION

The characteristics of high calorific value and environmental friendliness of hydrogen energy make it one of the most potential energy sources [1–3]. As a green and sustainable method to produce hydrogen in electrochemical water decomposition, hydrogen evolution reaction (HER, $2H^+ + 2e^- \rightarrow H_2$) has become an intriguing subject in recent years [4–6]. Pure metals, such as Pt, Ru, Rh, Ir, and Pd, and the related alternative materials in terms of monoatomic catalyst and various compounds [7–16] are proposed as HER catalysts. Notably, the commercial application of precious metal is limited by their scarcity and cost [17–19] and the activity and stability of conventional substitutions need to be improved [7–16]. Hence the stable, efficient, and economical HER catalysts are still desired.

Accompanied by the research on topological quantum materials, topological semimetals (TSMs) and topological insulators (TIs) are expected to act as HER catalysts, which benefit from the nontrivial band topology protected topological surface states (TSS). Such nontrivial TSS is relatively stable to mild impurities (magnetic/nonmagnetic), surface oxidation, and degradation [20–22]. As for TSMs, the effective catalyst candidates for HER are reported in the Weyl semimetals [23,24], Dirac semimetals [25–27], chiral nodal point semimetals [28], nanoporous electride with multifold fermions [29], and nodal-line semimetals [30–32]. The electrocatalytic activity of TSMs might mainly ascribe to their high carrier mobility and the large surface density of states near the Fermi level E_F, both of which are closely related to the TSS [33–35]. Referring to the TIs, an ideal TI, such as the well-known Bi_2Se_3 where only TSS crosses the E_F [36], tends not to be a good electrocatalyst [37–41] and this might attribute to the lower carrier density around E_F [30]. To increase the surface carrier and hence improve the catalytic efficiency of TIs, strain [42], atom/cluster embellishment [37], TI heterostructure construction [38–40] and surface engineering in terms of interfaces and grain boundaries [41,43], and partially oxidized surface [40,44] are introduced. Then, one may ask if there is any TI with inherently excellent HER performance. Here, we point out that the metal-like TIs, such as Li_2Pt and Li_2Pd, would be ideal catalysts for HER.

Here, we propose the hexagonal Li_2Pt family of materials (space group $P6/mmm$) (Fig. 1) has excellent HER performance stimulated by the intrinsic nontrivial TSS. Taking Li_2Pt as an example, one can find two sets of nodal net emerge around the $k_z = 0$ and $k_z = \pi$ plane when spin polarization is excluded. When SOC is considered, the nodal nets vanish and yield a strong TI with $\mathbb{Z}_2$ index $(\nu_0; \nu_1, \nu_2, \nu_3) = (1; 0, 0, 0)$. The nontrivial TSS cover a large energy range and wide area in surface Brillouin zone (BZ) [Fig. 2(g)], which suggests Li_2Pt might have potential catalytic properties [24,31,34]. By adsorbing one H atom on the layer substrate, the calculated ΔG_{H^*} for the top site [Fig. 3(b)] and bridge site [Fig. 3(c)] is as low as 0.187 eV and 0.054 eV (Table I), respectively. The

*madason.xin@gmail.com
†xiaotianwang@swu.edu.cn
‡mqkuang@swu.edu.cn

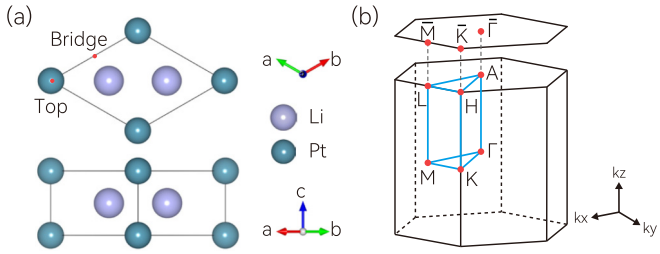

FIG. 1. (a) Top and side view of Li_2Pt. The top and bridge adsorption sites are highlighted by the red points in the top panel. (b) The Brillouin zone of Li_2Pt, in which the high symmetry points and the projected (001) plane are illustrated.

isostructural compound Li_2Pd is also identified as a strong TI with a ΔG_{H^*} value of 0.641 eV and 0.041 eV for the top site and bridge site in the eight-layer slab, respectively. It is worth noting that the HER activity (the value of ΔG_{H^*}) of the bridge site in Li_2Pt (0.054 eV) and Li_2Pd (0.041 eV) is superior to that of Pt (−0.09 eV) [45]. The excellent HER behavior of the bridge site as well as the different catalytic activity between the top site and bridge site as ascribed to H hybridizes with the nontrival TSS at the bridge site while this hardly happens at the top site. This work unveils the efficient HER catalytic properties in strong TIs and demonstrates the vital role of TSS in improving the HER performance.

II. COMPUTATIONAL METHODS

We carried out first-principles calculations by the Vienna *Ab initio* Simulation Package (VASP) [46] within the framework of the density-functional theory (DFT) [47]. The exchange-correlation potential was set as the generalized gradient approximation (GGA) of the Perdew-Burke-Ernzerhof (PBE) type [48]. The energy cutoff was set as 500 eV and the BZ was sampled via a Monkhorst-Pack k mesh with a size of $18 \times 18 \times 25$. For the structure optimization calculations, the convergence criteria of energy and force were set to 10^{-6} eV/atom and −0.01 eV/Å, respectively. The dynamical stability of the $2 \times 2 \times 2$ supercell was illustrated by the phonon dispersion from the density functional perturbation theory (DFPT) within the PHONOPY package [49] [Fig. S24 in the Supplemental Material (SM) [50]]. The TSS was demonstrated based on the maximally localized Wannier functions [51] and the WANNIERTOOLS package [51,52].

TABLE I. Calculated ΔE_{ads} (eV), ΔG_{H^*} (eV), and Bader charge of H (B_H, in e^-) for $Li_2Pt1 \times 1 \times n$ layer slab with SOC.

Site	Top			Bridge		
n	ΔE_{ads}	ΔG_{H^*}	B_H	ΔE_{ads}	ΔG_{H^*}	B_H
5	0.131	0.351	1.069	−0.147	0.073	1.274
6	0.100	0.320	1.072	−0.153	0.067	1.271
7	0.031	0.251	1.043	−0.162	0.058	1.269
8	−0.033	0.187	1.042	−0.166	0.054	1.270
9	−0.029	0.191	1.077	−0.154	0.066	1.279
10	0.022	0.242	1.079	−0.141	0.079	1.279
20	0.015	0.235	1.047	−0.160	0.060	1.270

For the catalytic properties calculations [24,31,34], the convergence criteria of energy and force was set as 10^{-4} eV/atom and −0.02 eV/Å, respectively. To illustrate the HER activity, $1 \times 1 \times n$ ($n = 5$–10) layer slab was constructed to adsorb H, where the vacuum layer was set to 16 Å to avoid the interaction between the layers. The stability of the layer slabs was confirmed by the calculated surface energies [28,53] (Table S1 [50]). The activity of HER can be characterized by the the Gibbs free energy ΔG_{H^*} (* denotes an active site on the surface and H* is the reaction intermediate). In this work, we adopted the method proposed by Norskov *et al.* to obtain the ΔG_{H^*} of hydrogen adsorption [54] . The specific process can be expressed as $H^+ + e^- \rightarrow H^*$ and $H^* \rightarrow 1/2H_2$. It is noted that the potential U is set to 0, corresponding to the standard hydrogen electrode at pH = 0, and the free energy of $H^+ + e^-$ is defined the same as that of $\frac{1}{2}H_2$ under standard conditions of equilibrium [54]. Then, the $\Delta G_{H^*} = \Delta E_{ads} + \Delta E_{ZPE} - T\Delta S_H$, in which ΔE_{ads} stands for the adsorption energy for H, ΔE_{ZPE} indicates the changes in zero-point energy, ΔS_H represents the entropy between the absorbed H and gaseous H, and T is the temperature (298.15 K) [54]. Particularly, the adsorption energy $\Delta E_{ads} = E_{slab+H} - E_{slab} - 1/2E_{H_2}$, in which E_{H_2}, E_{slab}, and E_{slab+H} are the energies of H_2, Li_2Pt without hydrogen, and Li_2Pt with adsorbed hydrogen, respectively. The calculated ΔE_{ZPE} is 0.022 eV, which agrees well with the previous result [54]. $\Delta S_H \approx -1/2S_H^0$, where S_H^0 is the entropy of gaseous H_2 at standard conditions [54]. As a result, $\Delta G_{H^*} = \Delta E_{ads} + 0.22$ eV for the Li_2Pt (001) surface. Besides, the aqueous solvent effect that might affect the energetic of electrochemical system [57,58] was evaluated by VASPSOL within an implicit continuum model [59,60]. The calculated results for the water solvent indicated the changes in ΔG_{H^*} values were less than 2 meV for the two active sites displayed in Fig. 1(a) (0.1868 eV → 0.1853 eV for the top site and 0.0540 eV → 0.0522 eV for the bridge site, respectively). Such a tiny variation indicates the water solvent has no significant effect on the catalytic performance of Li_2Pt. As a consequence, the solvent effect was reasonably omitted in our calculations. Moreover, the adsorption of intermediate OH^-, which has an importance effect on the energy barrier of H_2O dissociation in the alkaline conditions [61–64], was tested for the $Li_2Pt1 \times 1 \times n$ ($n = 5$–10) slab. It was found that the adsorption energy of OH* at the bridge and top site was respectively close to that of Pt and Ru [62] (see Table S2 [50]), suggesting a strong adsorption of OH* at the surface. Compared with the adsorption energy of H*, the adsorption energy of OH* is relatively strong, and there is no delicate balance between the adsorption rate of H* and desorption rate of OH*. Therefore, Li_2Pt might have a poorer HER performance in the alkaline conditions [61–64] than the acid ones with which we are concerned.

Although more accurate band structures could be acquired by the HSE06 functionals [65] and more accurate total energies might be obtained by the HSE06 [65] and random phase approximation (RPA) calculations for certain cases [64], the GGA-PBE [48] method is still a good description for most band dispersion and total energy calculations, whose validity and efficiency have been widely confirmed in the DFT calculations for topological quantum catalysts (TQCs) [23–35]. Therefore, all the DFT calculations in this work were com-

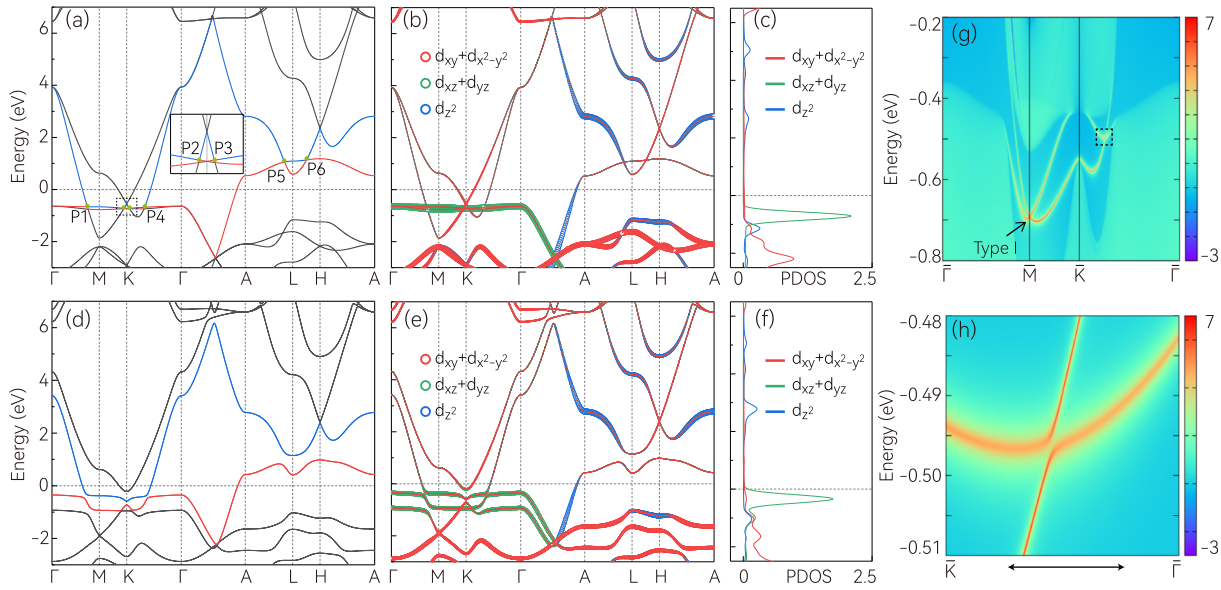

FIG. 2. Calculated band structures of Li_2Pt without spin polarization (a) and with SOC (d). The red and blue lines indicate the valence band (VB) and the conduction band (CB), respectively. The green points in (a) highlight the BCPs numbered as P1–P6. The inset is an enlarged view for the BCPs in the dashed rectangle. The *d*-orbital resolved band structures and the corresponding PDOSs for Li_2Pt without spin polarization [(b) and (c)] and with SOC [(e) and (f)], respectively. (g) The calculated surface states along selected paths on the (001) surface for Li_2Pt. (h) The enlarged image for the dotted rectangle in (g).

puted within GGA-PBE scenarios for the sake of accuracy requirement and time consumption.

III. RESULTS AND DISCUSSION

A. Electronic structure and symmetry analysis

The structure of Li_2Pt is displayed in Fig. 1(a), in which Pt and Li take up the 1*a* (0,0,0) and 2*d* (1/3,2/3,1/2) Wckyoff positions of space group *P*6/*mmm* (No. 191), respectively. Figure 2(a) shows the calculated spinless band structures based on the optimized crystal lattice, in which $a = b = 4.186$ Å and $c = 2.680$ Å agree well with the experimental values $a = b = 4.186$ Å and $c = 2.661$ Å [66]. Then, one can find six band crossing points (BCPs), labeled as P1–P6, along the high symmetry lines Γ-M-K-Γ-A-L-H-A [Fig. 1(b)]. As shown in Figs. S2– S16 [50] (see SM for detailed

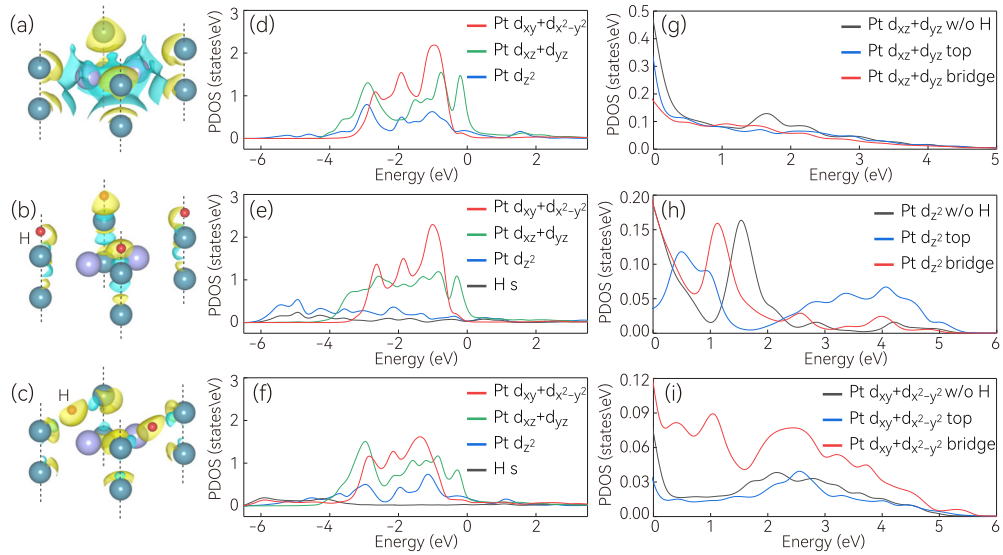

FIG. 3. Charge density difference for Li_2Pt eight-layer bulk without H adsorption (a), eight-layer slab with H adsorption on the top site (b), and eight-layer slab with H adsorption on the bridge site (c). The charge accumulation and depletion is indicated by the yellow and cyan region, respectively. The isosurface is set as 0.009 electrons/Å^{-3} (a) and 0.006 electrons/Å^{-3} [(b) and (c)], respectively. The displayed thickness is set to one unit cell. Panels (d), (e), and (f) are the PDOSs of Pt *d* and H *s* orbitals on the top layer of (001) surface corresponding to (a), (b), and (c), respectively. Panels (g), (h), and (i) are the hole density of states of Pt $d_{xz} + d_{yz}$, d_{z^2}, $d_{xy} + d_{x^2-y^2}$ and H *s* orbitals on the top layer of (001) surface, respectively.

illustration), these BCPs belong to two nodal nets near the $k_z = 0$ and $k_z = \pi$ plane, respectively. When the intrinsic SOC effect is considered, the system turns to a metal state with local band gap in the whole BZ, as shown in Fig. 2(d). The orbital resolved band structures and projected density of states (PDOSs) (Fig. 2 and Fig. S1 [50]) indicate the band inversion arises from the Pt $d_{xz} + d_{yz}$ and $d_{x^2-y^2} + d_{xy}$ orbitals at K point. The topological states on the (001) surface and surface Dirac cone at $\overline{\mathrm{M}}$ are clearly illustrated in Figs. 2(g) and 2(h) (also see Fig. S17 [50]).

To fully interpret the nontrivial TSS, we calculated the topological symmetry indexes (SI) of this system. The SI of SG $P6/mmm$ form the group $\mathbb{Z}_6 \times \mathbb{Z}_{12}$ [67] and the calculated result is $(\mathrm{Z}_6, \mathrm{Z}_{12}) = (3, 3)$. The odd values of $(\mathrm{Z}_6, \mathrm{Z}_{12})$ correspond to the strong TI phase, which is further evaluated by the $\mathbb{Z}_2$ topological invariant $(\nu_0; \nu_1, \nu_2, \nu_3) = (1; 0, 0, 0)$ for the occupied band of Li_2Pt. Hence, when projected to the (001) surface, there would be odd numbers of surface Dirac cone at the time reversal invariant points, which is protected by the time reversal symmetry. As for Li_2Pt, the surface Dirac cone locates at the $\overline{\mathrm{M}}$ point in the surface BZ [Fig. 2(g)]. Noteworthily, there seems to be a surface Dirac cone along the high symmetry line $\overline{\Gamma}$-$\overline{\mathrm{K}}$ [see the dashed rectangle in Fig. 2(g)]. Physically, the symmetry protection mechanism of such a surface Dirac cone is absent. To verify this point, the zoom in image is shown in Fig. 2(h), where a narrow band gap is observed.

B. HER activity and underlying mechanism

In view of the fact that the band-topology-protected TSS can provide a stable electron bath with high carrier mobility [23–28,30,33–35,68], HER testing is carried out for Li_2Pt. The calculated HER activity characterized by the ΔG_{H^*} and ΔE_{ads} for the top site and bridge site [Fig. 1(a)] are summarized in Table I. As illustrated in Table I, the ΔE_{ads} and ΔG_{H^*} of the top site suffer a larger fluctuation than that of the bridge site for the given $1 \times 1 \times n$ (n = 5–10) layer slab. Noticeably, the ΔG_{H^*} of the top site (0.19–0.35 eV) and the bridge site, which ranges from 0.05 to 0.08 eV and reaches a minimum for the eight-layer slab (0.054 eV), is comparable and even superior to the reported transition metal catalysts and TQCs (see Table S3 [50] and Fig. 6) [23–25,27,28,31,45,69].

Before analyzing the role and effect of TSS in the HER catalytic performance, especially the difference between the top site and bridge site, we will first return to the classical d-band center theory [70,71] and Sabatier principle [4,69,72]. In general, the proton absorption at the active site is stronger when the d-band center is closer to the E_F [73]. Besides, the interaction between the adsorbate and substrate should be neither too strong nor too weak [4,69,72], i.e., a moderate bonding is beneficial to capture the adsorbate and dissociate the product. Here, we take the eight-layer slab which has the best HER performance for both the top site and bridge site (Table I) as an example to perform the following analysis. The calculated d-band center with SOC is 0.494 eV [74], suggesting the antibonding orbitals are partially above the E_F and the adsorption strength would be medium [73] (Table I).

To evaluate the bonding between H and the layer substrate of Li_2Pt, we computed the charge density difference, the PDOSs of the Pt d and H s orbitals, and the Bader charge analysis [75]. For the case without H adsorption, Pt obtains electrons from Li [Fig. 3(a)] and has an average value of -1.649 e$^-$, which can attribute to the larger electronegativity of Pt (2.2) than Li (0.98) [76]. When H is captured by the layer slab, H s orbital is closely hybridizing with the Pt d_{z^2} [Fig. 3(e)] and $d_{xy} + d_{x^2-y^2}$ orbital [Fig. 3(f)] for the top site and bridge site adsorption, respectively. As a consequence, the Pt d_{z^2} [Fig. 3(h)] and $d_{xy} + d_{x^2-y^2}$ [Fig. 3(i)] orbital donates the most electrons to the adsorbed H at the top site and bridge site, respectively [also see Fig. 3(g) where the electrons of the $d_{xz} + d_{yz}$ orbital slightly increase]. Besides, Figs. 3(e), 3(f), and Fig. S22 also indicate the H s orbital is more localized for the top site bonding, i.e., more peaks in the PDOS than that of the bridge site, suggesting a weaker interaction with the substrate [69] for the top site. As a consequence, the Bader charge of H (B_{H}) at the top site is less than that of the bridge one (Table I). Further Bader charge analysis (Table II) also reveals the surface Pt atom can afford the electrons that H captures. In particular, the number of electrons that H obtains is less than that which Pt donates, indicating the weak interaction between the bulk bands and H for both the top site and bridge site [69].

TABLE II. Bader charge analysis (B, in e$^-$) of the top-layer atoms in the eight-layer Li_2Pt and Li_2Pd slab with SOC. The charge differences Δ_C (e$^-$) are listed.

Site		w/o H	Top		Bridge	
Compound	Atom	B	B	Δ_C	B	Δ_C
Li_2Pt	Pt	11.145	11.050	−0.095	10.747	−0.398
	H		1.042	+0.042	1.270	+0.270
Li_2Pd	Pd	11.023	10.990	−0.033	10.599	−0.424
	H		1.081	+0.081	1.406	+0.406

Now, we will get back to the HER catalytic performance. It is noteworthy that the Pt $d_{xy} + d_{x^2-y^2}$ orbital participates in the band inversion, while the d_{z^2} orbital dose not (Fig. 2). Combined with the demonstrations for the bonding between H and Li_2Pt layer slabs (Fig. 3, Tables I and II), one can deduce that H hybridizes with the nontrival TSS at the bridge site in a medium degree, while H hardly hybridizes with the nontrival TSS at the top site. As a result, the change of ΔG_{H^*} due to the adsorption on the layer slab of varying thickness tends to be small and hence a better HER performance emerges at the bridge site (Table I).

To confirm the TSS indeed takes part in the HER process, one should figure out the distribution of the electron bath provided by the nontrivial TSS and evaluate the reconstruction of electron configuration after H adsorption. We calculated the slab band structures of the Li_2Pt (001) surface by the MLWFs [51] and DFT [47] method, respectively. The evolution of thickness-dependent slab band structures from the MLWFs (Fig. S18 [50]) indicate the TSS remains nearly unchanged until the slab layer reaches up to 20. Then, we take the surface electronic structures of the 20-layer slab as an illustration (Fig. 4). As shown in Figs. 4(a)–4(c), the nontrivial TSS (highlighted in red) is maintained after H adsorption for the top site and bridge site, respectively. The calculations for the real part

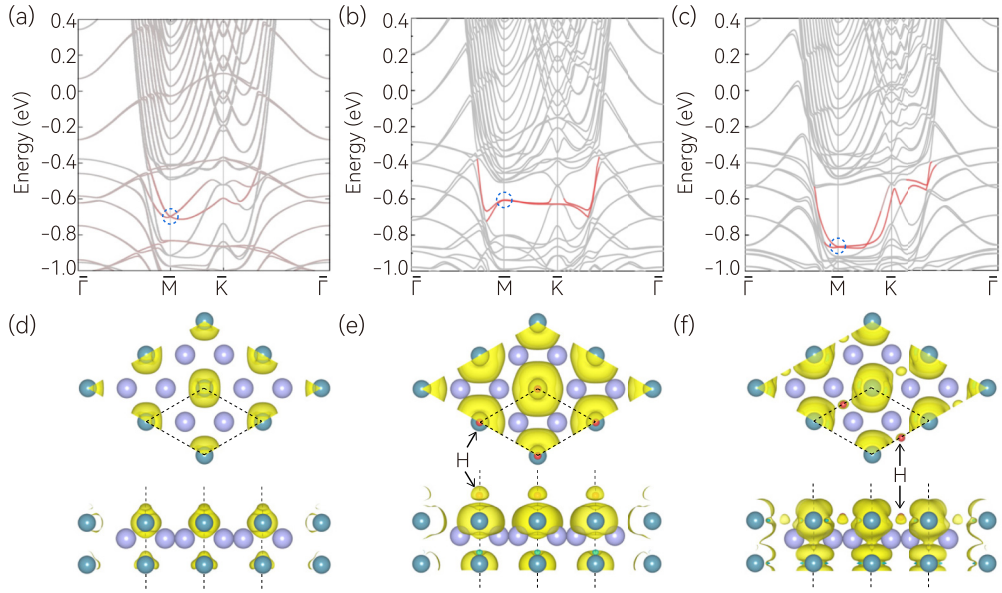

FIG. 4. Surface electronic structures of the (001) surface for Li_2Pt 20-layer slab without H adsorption from MLWFs (a) and with H adsorption on the top site (b) and bridge site (c) from DFT calculations, respectively. The red lines highlight the TSS. Panels (d), (e), and (f) are the real wave functions of the TSS at the $\overline{M}$ point as circled in blue in (a), (b), and (c), respectively. The isosurface is set to 0.0003 electrons/Å^{-3}. The displayed thickness is set to one unit cell. The adsorbed H atoms are indicated by the black arrows in (e) and (f).

of the wave function at the $\overline{M}$ point suggest the distinct charge transfer between the TSS and H [Figs. 4(d)–4(f)]. Besides, the calculated ΔE_{ads}, ΔG_{H^*}, and B_H are listed in Table I. One can find the bridge site ($\Delta G_{H^*} = 0.06$ eV) still reveals a better HER activity than the top site ($\Delta G_{H^*} = 0.235$ eV), which can ascribe to the moderate hybridization between H and the Pt $d_{xy} + d_{x^2-y^2}$ orbital at the bridge site (Fig. 3 and Fig. S23 [50]). Then, we may conclude the HER activity at the top site, in which H interacts with the Pt d_{z^2} orbital (Fig. 3, Fig. S21, and Fig. S23 [50]), is closely related to the surface electrons that withhold contributions to TSS; the HER activity at the bridge site, in which H interplays with the Pt $d_{xy} + d_{x^2-y^2}$ orbital (Fig. 3, Fig. S21, and Fig. S23 [50]), is dominated by the topological electron bath.

Following the above design route, the isostructural Li_2Pd [77] is also identified as a strong TI with efficient HER catalytic activity. Figure S20 [50] reveals the surface Dirac cone emerges at $\overline{M}$ in the surface spectrum and the TSS spreads a wide energy window and large area in surface BZ, which is similar to Li_2Pt [Fig. 2(g)]. For the sake of simplicity, we make an estimation of the ΔG_{H^*} for a $1 \times 1 \times 8$ layer slab. The calculated d-band center is 0.658 eV, which is above the E_F and higher than that of Li_2Pt (0.494 eV). As a result, the higher antibonding orbitals yield a larger ΔE_{ads} [54,70,71] for the top site (0.421 eV) and bridge site (−0.179 eV), respectively. The calculated ΔG_{H^*} respectively approaches 0.641 eV for the top site and 0.041 eV for the bridge site, suggesting the bridge site has an efficient HER activity [23,24,28,31].

As shown in Figs. 5(e), 5(f), and Fig. S21 [50], the H s orbital is highly hybridizing with the Pd d_{z^2} and $d_{xy} + d_{x^2-y^2}$ orbital for the top site [Fig. 5(b)] and bridge site [Fig. 5(c)] adsorption, respectively. The band structures (Fig. S19 [50]) also indicates the TSS comes from the band inversion between Pd $d_{xz} + d_{yz}$ and $d_{xy} + d_{x^2-y^2}$ orbitals. Analogous to Li_2Pt, one can safely infer that the HER activity at the top site and bridge site is dominated by the nontopological and topological surface electrons, respectively. Moreover, the Bader charge analysis (Table II) reveals the surface Pd provides enough electrons to the H adataom at the bridge site, while the surface Pd could not afford the electrons that H requires at the top site (also see the hole DOSs in Fig. 5). Actually, for the top site, more than half of the electrons that H received come from the bulk states, i.e., H acquired 0.081 electrons from the Li_2Pd layer slab where the top-layer atoms supplied 0.033 electrons and the remaining 0.048 electrons come from the bulk (Table II). Besides, one can find a large and sharp DOS peak around −4.4 eV in Fig. 5(e) and Fig. S21 [50], suggesting a strong hybridization between the H s and Pt d_{z^2} orbitals. Combining the Bader analysis (Table II) with the PDOS [Fig. 5(e) and Fig. S21 [50]], one can deduce that H is bonding and interacting with the bulk states in a strong degree for the top site. Such a strong interaction would bring in a high ΔG_{H^*} [69] and the obtained ΔG_{H^*} is 0.641 eV for the top site of Li_2Pd, which is much larger than the top site of Li_2Pt (0.187 eV) where the interaction between H and the substrate is very weak.

In the end, we plot the sketch map for the HER process at the top site and bridge site for Li_2Pt [Figs. 6(a) and 6(b)]. Also the $|\Delta G_{H*}|$ diagram of HER and the volcano plot for the Li_2Pt and Li_2Pd eight-layer slab with bridge site absorption are shown in Figs. 6(c) and 6(d). It is clear that the ΔG_{H^*} of Li_2Pt and Li_2Pd are almost at the top of the volcanic curve, which is superior to most transition metal catalysts and other known TQCs [23,24,28,45] [Figs. 6(c), 6(d), and Table S3 [50]]. The efficient HER performance at the bridge site of the (001) surface for Li_2Pt and Li_2Pd is attributed to the intermediate hybridization between H and the surface electrons with high carrier mobility stemming from the nontrivial TSS [23–30,33–35,68,69].

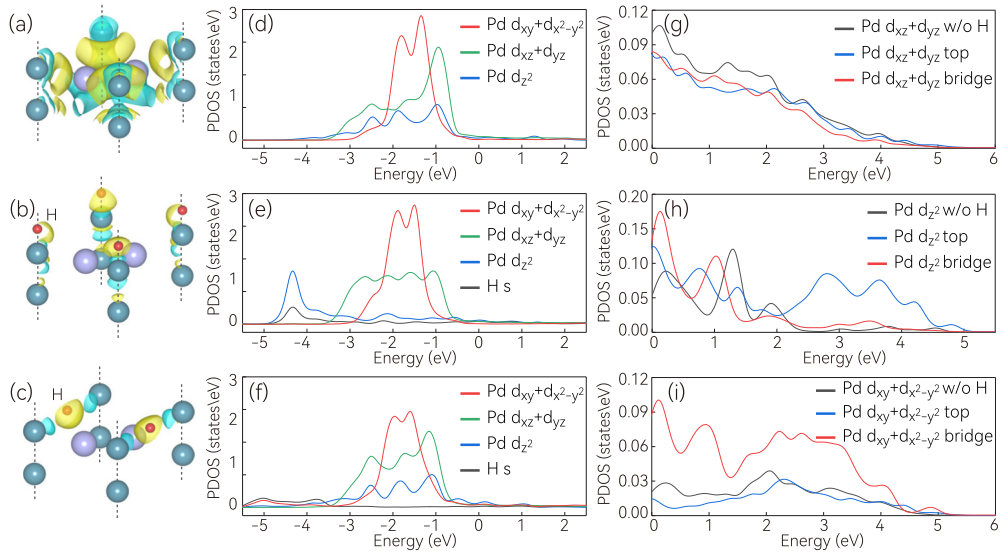

FIG. 5. Charge density difference for Li_2Pd eight-layer bulk without H adsorption (a), eight-layer slab with H adsorption on the top site (b), and eight-layer slab with H adsorption on the bridge site (c). The charge accumulation and depletion is indicated by the yellow and cyan region, respectively. The isosurface is set as 0.002 electrons/Å^{-3} (a) and 0.006 electrons/Å^{-3} [(b) and (c)], respectively. The displayed thickness is set to one unit cell. Panels (d), (e), and (f) are the PDOSs of Pd d and H s orbitals on the top layer of (001) surface corresponding to (a), (b), and (c), respectively. Panels (g), (h), and (i) are the hole density of states of Pd $d_{xz}+d_{yz}$, d_{z^2}, $d_{xy}+d_{x^2-y^2}$ and H s orbitals on the top layer of (001) surface, respectively.

IV. CONCLUSION

Unlike most TIs whose catalytic performance needs to be improved by either bringing in strain or covering metal atoms/clusters or introducing oxidized surface/surface vacancies/interfaces/grain boundaries or constructing heterostructrues with layered materials, the strong TIs Li_2Pt and Li_2Pd promote intrinsic efficient catalytic response to the HER at the bridge site. The high-efficiency HER performance of the bridge site can briefly ascribe to three aspects. First, a suitable d-band center ensures an appropriate adsorption energy [70,71,73]. Second, a considerably weak interaction between H and the substrate is beneficial to capture the adsorbate and dissociate the product [4,69,72]. Third, a moderate hybridization between H and the TSS offers an efficient charge transfer for catalytic action [69]. Specially, the TSS should first cover the specific active sites and hence act as a constituent part of the surface electron bath where the HER reacts [Figs. 4(e) and 4(f)]; second and more importantly, the TSS should interact with the adsorbate in an appropriate degree [Figs. 3(e), 3(f), 5(e), 5(f) and Fig. S21 [50]] to support the ultrafast charge transfer which is conducive to the HER. The above three points guarantee the adsorption activity and give birth to a subtle cooperative effect [61,72,78], yielding a high-efficiency HER catalytic performance. Our work brings an insight into the enhancement of catalytic activity by TSS and provides a feasible scheme for TQCs design, i.e., the bottleneck of TIs serving as electrocatalysts from the lower carrier density around E_F [30] might be conquered by a cooperative effect.

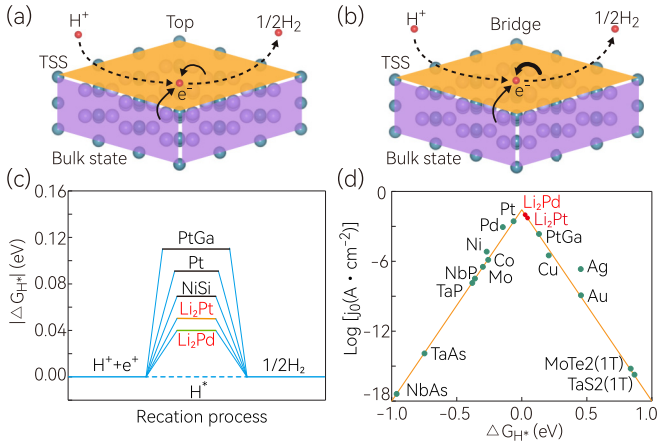

FIG. 6. (a), (b) Sketch map for the HER activity on the top and bridge site of Li_2Pt, respectively. The bigger solid arrow indicates the stronger interaction between H and the TSS/substrate. (c) The $|\Delta G_{H*}|$ diagram of HER. The data of NiSi, Pt, and PtGa are taken from the literature [24,28,45]. (d) The volcano plot for the HER of Li_2Pt and Li_2Pd in comparison with that of various transition metal catalysts and TQCs [23,28]. The data of Li_2Pt and Li_2Pd corresponds to the eight-layer slab with bridge site absorption.

ACKNOWLEDGMENTS

Y.-H.W. acknowledges helpful discussions with N. S. Liu and J. L. Gong. This work was supported by the Natural Science Foundation of China (NSFC, Grants No. 11704315 and No. 12204074). D.-S.M. also acknowledges the financial support from the China National Postdoctoral Program for Innovative Talent (Grant No. BX20220367). Part of the work was performed on the high performance-computing platform of School of Physical Science and Technology of Southwest University.

[1] J. A. Turner, Science **305**, 972 (2004).
[2] X. Wang, K. Maeda, A. Thomas, K. Takanabe, G. Xin, J. M. Carlsson, K. Domen, and M. Antonietti, Nat. Mater. **8**, 76 (2009).
[3] J. Mahmood, M. A. R. Anjum, S.-H. Shin, I. Ahmad, H.-J. Noh, S.-J. Kim, H. Y. Jeong, J. S. Lee, and J.-B. Baek, Adv. Mater. **30**, 1805606 (2018).
[4] P. C. Vesborg, B. Seger, and I. Chorkendorff, J. Phys. Chem. Lett. **6**, 951 (2015).
[5] J. Sun, F. Tian, F. Yu, Z. Yang, B. Yu, S. Chen, Z. Ren, and H. Zhou, ACS Catal. **10**, 1511 (2020).
[6] X. X. Wang, M. T. Swihart, and G. Wu, Nat. Catal. **2**, 578 (2019).
[7] Y. Xu and M. A. Schoonen, Am. Mineral. **85**, 543 (2000).
[8] J. Greeley, I. Stephens, A. Bondarenko, T. P. Johansson, H. A. Hansen, T. Jaramillo, J. Rossmeisl, I. Chorkendorff, and J. K. Nørskov, Nat. Chem. **1**, 552 (2009).
[9] M. G. Walter, E. L. Warren, J. R. McKone, S. W. Boettcher, Q. Mi, E. A. Santori, and N. S. Lewis, Chem. Rev. **110**, 6446 (2010).
[10] J. Suntivich, K. J. May, H. A. Gasteiger, J. B. Goodenough, and Y. Shao-Horn, Science **334**, 1383 (2011).
[11] H. Vrubel and X. Hu, Angew. Chem. Int. Ed. **51**, 12703 (2012).
[12] M. W. Louie and A. T. Bell, J. Am. Chem. Soc. **135**, 12329 (2013).
[13] F. E. Osterloh, Chem. Soc. Rev. **42**, 2294 (2013).
[14] F. Dvořák, M. F. Camellone, A. Tovt, N.-D. Tran, F. R. Negreiros, M. Vorokhta, T. Skála, I. Matolínová, J. Mysliveček, V. Matolín *et al.*, Nat. Commun. **7**, 10801 (2016).
[15] Y. Shi and B. Zhang, Chem. Soc. Rev. **45**, 1529 (2016).
[16] J.-Y. Hwang, S.-T. Myung, and Y.-K. Sun, Chem. Soc. Rev. **46**, 3529 (2017).
[17] B. Conway and B. Tilak, Electrochim. Acta **47**, 3571 (2002).
[18] J. Greeley, T. F. Jaramillo, J. Bonde, I. Chorkendorff, and J. K. Nørskov, Nat. Mater. **5**, 909 (2006).
[19] X. Zou and Y. Zhang, Chem. Soc. Rev. **44**, 5148 (2015).
[20] D. Kong and Y. Cui, Nat. Chem. **3**, 845 (2011).
[21] J. Xiao, L. Kou, C.-Y. Yam, T. Frauenheim, and B. Yan, ACS Catal. **5**, 7063 (2015).
[22] A. Politano, G. Chiarello, C.-N. Kuo, C. S. Lue, R. Edla, P. Torelli, V. Pellegrini, and D. W. Boukhvalov, Adv. Funct. Mater. **28**, 1706504 (2018).
[23] C. R. Rajamathi, U. Gupta, N. Kumar, H. Yang, Y. Sun, V. Süß, C. Shekhar, M. Schmidt, H. Blumtritt, P. Werner, B. Yan, S. Parkin, C. Felser, and C. N. R. Rao, Adv. Mater. **29**, 1606202 (2017).
[24] W. Liu, X. Zhang, W. Meng, Y. Liu, X. Dai, and G. Liu, iScience **25**, 103543 (2022).
[25] G. Li, C. Fu, W. Shi, L. Jiao, J. Wu, Q. Yang, R. Saha, M. E. Kamminga, A. K. Srivastava, E. Liu *et al.*, Angew. Chem. **131**, 13241 (2019).
[26] Q. Yang, C. Le, G. Li, T. Heine, C. Felser, and Y. Sun, Appl. Mater. Today **22**, 100921 (2021).
[27] X.-P. Kong, T. Jiang, J. Gao, X. Shi, J. Shao, Y. Yuan, H.-J. Qiu, and W. Zhao, J. Phys. Chem. Lett. **12**, 3740 (2021).
[28] Q. Yang, G. Li, K. Manna, F. Fan, C. Felser, and Y. Sun, Adv. Mater. **32**, 1908518 (2020).
[29] W. Meng, X. Zhang, Y. Liu, X. Dai, G. Liu, Y. Gu, E. Kenny, and L. Kou, Adv. Sci. **10**, 2205940 (2022).
[30] J. Li, H. Ma, Q. Xie, S. Feng, S. Ullah, R. Li, J. Dong, D. Li, Y. Li, and X.-Q. Chen, Sci. China Mater. **61**, 23 (2018).
[31] L. Wang, X. Zhang, W. Meng, Y. Liu, X. Dai, and G. Liu, J. Mater. Chem. A **9**, 22453 (2021).
[32] X. Zhang, L. Wang, M. Li, W. Meng, Y. Liu, X. Dai, G. Liu, Y. Gu, J. Liu, and L. Kou, Mater. Today (2023), doi:10.1016/j.mattod.2023.05.002.
[33] S. Wang, B.-C. Lin, A.-Q. Wang, D.-P. Yu, and Z.-M. Liao, Adv. Phys.: X **2**, 518 (2017).
[34] L. Wang, Y. Yang, J. Wang, W. Liu, Y. Liu, J. Gong, G. Liu, X. Wang, Z. Cheng, and X. Zhang, EcoMat **5**, e12316 (2022).
[35] H. Luo, P. Yu, G. Li, and K. Yan, Nat. Rev. Phys. **4**, 611 (2022).
[36] H. Zhang, C.-X. Liu, X.-L. Qi, X. Dai, Z. Fang, and S.-C. Zhang, Nat. Phys. **5**, 438 (2009).
[37] H. Chen, W. Zhu, D. Xiao, and Z. Zhang, Phys. Rev. Lett. **107**, 056804 (2011).
[38] L. Li, J. Zeng, W. Qin, P. Cui, and Z. Zhang, Nano Energy **58**, 40 (2019).
[39] G. Li, J. Huang, Q. Yang, L. Zhang, Q. Mu, Y. Sun, S. Parkin, K. Chang, and C. Felser, J. Energy Chem. **62**, 516 (2021).
[40] Q. Qu, B. Liu, W. S. Lau, D. Pan, and I. K. Sou, Cell Rep. Phys. Sci. **4**, 101332 (2023).
[41] S. Izadi, J. W. Han, S. Salloum, U. Wolff, L. Schnatmann, A. Asaithambi, S. Matschy, H. Schlörb, H. Reith, N. Perez *et al.*, Small **17**, 2103281 (2021).
[42] R. M. Sattigeri, P. K. Jha, P. Śpiewak, and K. J. Kurzydłowski, Appl. Phys. Lett. **121**, 123101 (2022).
[43] H. Xie, T. Zhang, R. Xie, Z. Hou, X. Ji, Y. Pang, S. Chen, M.-M. Titirici, H. Weng, and G. Chai, Adv. Mater. **33**, 2008373 (2021).
[44] Q. Qu, B. Liu, J. Liang, H. Li, J. Wang, D. Pan, and I. K. Sou, ACS Catal. **10**, 2656 (2020).
[45] B. Hinnemann, P. G. Moses, J. Bonde, K. P. Jørgensen, J. H. Nielsen, S. Horch, I. Chorkendorff, and J. K. Nørskov, J. Am. Chem. Soc. **127**, 5308 (2005).
[46] G. Kresse and D. Joubert, Phys. Rev. B **59**, 1758 (1999).
[47] M. C. Payne, M. P. Teter, D. C. Allan, T. A. Arias, and J. D. Joannopoulos, Rev. Mod. Phys. **64**, 1045 (1992).
[48] J. P. Perdew, K. Burke, and M. Ernzerhof, Phys. Rev. Lett. **77**, 3865 (1996).
[49] A. Togo and I. Tanaka, Scr. Mater. **108**, 1 (2015).
[50] See Supplemental Material at http://link.aps.org/supplemental/10.1103/PhysRevB.107.235414 for the following: projected band structures and density of states of Li_2Pt; sketch map of seven nodal rings and topological surface states of Li_2Pt without SOC; surface electronic band structures of Li_2Pt; projected band structures, density of states and topological surface states of Li_2Pd; comparison of the density of states for the Pt/Pd d_{z^2} ($d_{xy} + d_{x^2-y^2}$) and H s orbital for the top (bridge) site adsorption; comparison of the density of states for the H s orbital for the top (bridge) site adsorption on the (001) surface of Li_2Pt and Li_2Pd $1 \times 1 \times 8$ layer slab; the PDOSs of Pt d and H s orbitals on the top layer of (001) surface for Li_2Pt 20-layer slab; the phonon dispersion of Li_2Pt; the surface energies of Li_2Pt $1 \times 1 \times n$ ($n = 2$–10, 20) layer slab; the adsorption energy of OH molecule on the Li_2Pt $1 \times 1 \times n$ ($n = 5$–10) slab; the Gibbs free energy ΔG_{H^*} of the reported transition metal catalysts and topological quantum catalysts. The Supplemental Material also contains Refs. [18,23–31,38,40,42,44,53–56].
[51] A. A. Mostofi, J. R. Yates, Y.-S. Lee, I. Souza, D. Vanderbilt, and N. Marzari, Comput. Phys. Commun. **178**, 685 (2008).

[52] Q. Wu, S. Zhang, H.-F. Song, M. Troyer, and A. A. Soluyanov, Comput. Phys. Commun. **224**, 405 (2018).
[53] Q. Li, M. Rellán-Piñeiro, N. Almora-Barrios, M. Garcia-Ratés, I. N. Remediakis, and N. López, Nanoscale **9**, 13089 (2017).
[54] J. K. Nørskov, T. Bligaard, A. Logadottir, J. Kitchin, J. G. Chen, S. Pandelov, and U. Stimming, J. Electrochem. Soc. **152**, J23 (2005).
[55] S. Trasatti, J. Electroanal. Chem. Interfacial Electrochem. **39**, 163 (1972).
[56] J. K. Nørskov, J. Rossmeisl, A. Logadottir, L. Lindqvist, J. R. Kitchin, T. Bligaard, and H. Jonsson, J. Phys. Chem. B **108**, 17886 (2004).
[57] L. Yu, X. Pan, X. Cao, P. Hu, and X. Bao, J. Catal. **282**, 183 (2011).
[58] Y. Sha, T. H. Yu, Y. Liu, B. V. Merinov, and W. A. Goddard, III, J. Phys. Chem. Lett. **1**, 856 (2010).
[59] K. Mathew, R. Sundararaman, K. Letchworth-Weaver, T. Arias, and R. G. Hennig, J. Chem. Phys. **140**, 084106 (2014).
[60] K. Mathew, V. Kolluru, S. Mula, S. N. Steinmann, and R. G. Hennig, J. Chem. Phys. **151**, 234101 (2019).
[61] Z. W. Seh, J. Kibsgaard, C. F. Dickens, I. Chorkendorff, J. K. Nørskov, and T. F. Jaramillo, Science **355**, eaad4998 (2017).
[62] Y. Zheng, Y. Jiao, A. Vasileff, and S.-Z. Qiao, Angew. Chem. Int. Ed. **57**, 7568 (2018).
[63] Z. Zhou, Z. Pei, L. Wei, S. Zhao, X. Jian, and Y. Chen, Energy Environ. Sci. **13**, 3185 (2020).
[64] M. Chen, T. J. Smart, S. Wang, T. Kou, D. Lin, Y. Ping, and Y. Li, J. Mater. Chem. A **8**, 8783 (2020).
[65] T. Ouahrani, R. M. Boufatah, M. Benaissa, Á. Morales-García, M. Badawi, and D. Errandonea, Phys. Rev. Mater. **7**, 025403 (2023).
[66] W. Bronger, B. Nacken, and K. Ploog, J. Less-Common Met. **43**, 143 (1975).
[67] Z. Song, T. Zhang, Z. Fang, and C. Fang, Nat. Commun. **9**, 3530 (2018).
[68] G. Li, Q. Xu, W. Shi, C. Fu, L. Jiao, M. E. Kamminga, M. Yu, H. Tüysüz, N. Kumar, V. Süß, R. Saha, A. K. Srivastava, S. Wirth, G. Auffermann, J. Gooth, S. Parkin, Y. Sun, L. Enke, and C. Felser, Sci. Adv. **5**, eaaw9867 (2019).
[69] M.-C. Jiang, G.-Y. Guo, M. Hirayama, T. Yu, T. Nomoto, and R. Arita, Phys. Rev. B **106**, 165120 (2022).
[70] J. Norsko, Rep. Prog. Phys. **53**, 1253 (1990).
[71] J. Nørskov, Prog. Surf. Sci. **38**, 103 (1991).
[72] R. Schlögl, Angew. Chem. Int. Ed. **54**, 3465 (2015).
[73] T. Bligaard and J. K. Nørskov, Electrochim. Acta **52**, 5512 (2007).
[74] V. Wang, N. Xu, J.-C. Liu, G. Tang, and W.-T. Geng, Comput. Phys. Commun. **267**, 108033 (2021).
[75] G. Henkelman, A. Arnaldsson, and H. Jónsson, Comput. Mater. Sci. **36**, 354 (2006).
[76] W. M. Haynes, *CRC Handbook of Chemistry and Physics* (CRC Press, Boca Raton, FL, 2016).
[77] O. Loebich, Jr. and C. J. Raub, J. Less-Common Met. **55**, 67 (1977).
[78] T. F. Jaramillo, K. P. Jørgensen, J. Bonde, J. H. Nielsen, S. Horch, and I. Chorkendorff, Science **317**, 100 (2007).